Chemical Engineering Research and Design 227 (2026) 879–893

Contents lists available at ScienceDirect

Chemical Engineering Research and Design

journal homepage: www.elsevier.com/locate/cherd

MRI-validated CFD–DEM simulation and recurrence-based time extrapolation (rCFD) of a bubbling fluidized bed: Drag model selection and computational speed-up ☆

Asif Shaik [a,*], Swantje Pietsch-Braune [a], Stefan Pirker [b], Melis Özdemir [c], Muhammad Adrian [c], Alexander Penn [c], Stefan Heinrich [a]

[a] Institute of Solids Process Engineering and Particle Technology, Hamburg University of Technology, Denickestraße 15, Hamburg, 21073, Germany
[b] Department of Particulate Flow Modelling, Johannes Kepler University, Altenbergerstraße 66a, Linz, 4040, Austria
[c] Institute of Process Imaging, Hamburg University of Technology, Denickestraße 17, Hamburg, 21073, Germany

ARTICLE INFO

Dataset link: https://hdl.handle.net/11420/57789, https://doi.org/10.15480/882.15949

Keywords:
rCFD
CFD–DEM
MRI
Gas–solid fluidized bed
Time-extrapolation

ABSTRACT

CFD–DEM simulations of industrial fluidized beds suffer from a major computational bottleneck: simulating one second of physical time often requires hours of wall-clock time on modern computer hardware, with hundreds of processors, which makes long-term process analysis impractical. Recurrence-based CFD (rCFD) addresses this challenge by exploiting pseudo-periodic flow patterns to extrapolate short CFD–DEM simulations over extended time periods, but experimental validation of such time-extrapolated predictions has remained absent. To our knowledge, this is the first rigorous experimental validation of rCFD against internal full-field magnetic resonance imaging (MRI) measurement of a cylindrical fluidized bed (96 mm inner diameter, 600 mm height) operated with poppy seeds ($d_{32} = 1.16$ mm) at 1.5 u_{mf}.

First, CFD–DEM predictions were validated against MRI measurements by comparing four drag models (Koch & Hill, Di Felice, Gidaspow, Beetstra) across multiple metrics: bed expansion dynamics, bubble size distributions, radial particle distributions, and bubble rise velocities. The Koch & Hill model demonstrated superior agreement, capturing mean bed heights within a deviation of 0.9 cm of MRI data (17.7 cm vs. 16.8 cm respectively) and correctly predicting most of the bubble formation patterns observed experimentally. Fast Fourier Transform analysis of the validated CFD–DEM data revealed a characteristic recurrence period of 0.27 s, enabling construction of a 5 s rCFD database.

Time-extrapolated rCFD simulations to 10 s maintained excellent agreement with extended MRI measurements, preserving bed expansion behavior, bubble size–velocity correlations without drift or spurious behavior. The approach achieved a $4,050\times$ computational speed-up, reducing the wall-clock time from 4.5 h to 4 s per simulated physical second while pursuing predictive accuracy. This validated methodology enables previously intractable applications, including real-time process optimization, parametric design studies, and digital twin development for industrial fluidized bed setups.

1. Introduction

Fluidization describes the transition of a fixed bed of solid particles into a fluid-like state when a gas stream is introduced through a distributor plate at the bottom of the apparatus. When the upward drag force exceeds the gravitational force, particles become suspended and exhibit fluid-like behavior. The minimum superficial gas velocity required to achieve this transition is termed the minimum fluidization velocity (u_{mf}). Fluidized beds offer distinct advantages for industrial gas–solid processes: efficient solids handling, uniform temperature distribution, large interfacial area for mass transfer, and high heat transfer coefficients.

Fluidized bed technology has transformed chemical manufacturing, energy production, and materials processing over the past few decades. The technology enabled breakthrough processes including fluid catalytic cracking, coal gasification, polyolefin production, and pharmaceutical coating (Chew et al., 2022; Zapater et al., 2024). Superior mixing characteristics and particle–gas contact efficiency facilitate

☆ This article is part of a Special issue entitled: 'Granulation 2025' published in Chemical Engineering Research and Design.

* Corresponding author.
E-mail address: shaik.asif@tuhh.de (A. Shaik).

https://doi.org/10.1016/j.cherd.2026.02.039
Received 22 October 2025; Received in revised form 11 February 2026; Accepted 13 February 2026
Available online 19 February 2026

process intensification through reduced reaction steps and improved energy utilization (Wang et al., 2020; Wu et al., 2022). These advantages have made fluidized beds indispensable for industrial operations ranging from Fischer–Tropsch synthesis to wastewater treatment (Cai et al., 2020; Darweesh and Weis, 2024).

Fluidized bed granulation and coating processes are particularly important in pharmaceutical and food industries, where particle coating enables controlled release of active ingredients and protection against moisture, heat, and microbial contamination (da Silva et al., 2014). However, many industrial processes suffer from low product yield within desired property specifications, resulting in substantial energy consumption and material waste (Heinrich et al., 2002b,a, 2003). Understanding internal particle dynamics is therefore essential for optimizing process parameters that govern product quality and yield.

Computational Fluid Dynamics coupled with the Discrete Element Method (CFD–DEM) has emerged as the primary tool for simulating gas–solid fluidized beds, with applications spanning coating and granulation (Kieckhefen et al., 2022; Sen et al., 2014; Grohn et al., 2020), drying (De Munck et al., 2023; Lan et al., 2022; Azmir et al., 2020), heat and mass transfer (Sutkar et al., 2016; Wang et al., 2019; Zhang et al., 2020; Lei et al., 2023), and gasification (Ku et al., 2015). Despite these advances, two fundamental barriers limit the industrial application of CFD–DEM simulations. First, experimental validation of internal flow predictions remains severely constrained, limiting confidence in simulation results. Second, the extreme computational cost of millions of particles simulated over hours of operation renders real-time process optimization impossible. This work addresses both challenges by integrating MRI validation with recurrence-based CFD acceleration.

CFD–DEM simulations reveal internal flow features critical to reactor performance: bubble nucleation and coalescence patterns, particle contact networks, vortex structures, and segregation dynamics (Zhao et al., 2023; Zhou et al., 2022). These phenomena directly control mixing efficiency, heat and mass transfer rates, and reaction performance. However, experimental validation of these predictions remains severely limited. Traditional validation relies predominantly on global measurements of pressure drop, overall bed expansion, or exit gas composition, which provide little insight into internal flow structures (Munck et al., 2023).

Advanced tomographic techniques have emerged but suffer from fundamental limitations. Electrical Capacitance Tomography (ECT) provides limited spatial resolution (~10% of bed diameter) (Watson et al., 2024). Particle Image Velocimetry (PIV) requires transparent walls and is restricted to quasi-2D systems. X-ray and CT imaging offer high resolution but require specialized facilities and provide limited temporal resolution (Wang and Shen, 2022; Tu et al., 2021). Radar-based methods struggle with penetration in dense particle beds (Yan, 2016; Guío-Pérez et al., 2023). No existing technique simultaneously provides the spatial resolution, temporal resolution, and full three-dimensional field measurements needed to validate complex bubble dynamics and particle mixing in dense fluidized beds.

Magnetic Resonance Imaging (MRI) addresses these validation challenges by providing non-invasive, three-dimensional visualization of both gas and solid phases with high spatiotemporal resolution. The vertical MRI system at Hamburg University of Technology among the few worldwide capable of 3D fluidized beds, captures previously inaccessible internal dynamics including bubble formation, coalescence, and particle clustering with 4 by 8 mm spatial and 20 ms temporal resolution (Penn et al., 2017; Clarke et al., 2025). Unlike other tomographic techniques, MRI simultaneously resolves gas bubbles (as signal voids) and particle-dense regions throughout the entire bed volume, enabling quantitative measurement of bubble size distributions, rise velocities, and formation frequencies at multiple bed heights. This experimental capability allows direct validation of CFD–DEM predictions, particularly the evaluation of drag models and contact models against measured bubble dynamics and flow patterns.

The second fundamental barrier to industrial CFD–DEM implementation is the prohibitive computational cost. Pilot and industrial-scale fluidized beds contain billions of particles operating over hours or days, yet current CFD–DEM simulations require months of high-performance computing time to simulate seconds of physical operation (Kieckhefen et al., 2019). This bottleneck arises from inherent multi-scale physics: DEM requires microsecond time steps to resolve particle collisions while industrial processes operate over hours, creating nine orders of magnitude temporal scale separation. Combined with $O(N^2)$ scaling of contact detection algorithms and the requirement to resolve fluid flow at sub-particle scales, even modern supercomputers cannot simulate industrial-scale systems. Various model reduction strategies have emerged, including CFD-based compartment models that decouple flow and population balance calculations (Weber et al., 2019), and Proper Orthogonal Decomposition (POD) methods that capture dominant flow features in reduced-dimensional spaces (Lucia et al., 2004; Jung et al., 2011; Raveh, 2001; Zhong et al., 2020; Li et al., 2024). However, compartment models sacrifice critical spatial information through time-averaging (Jourdan et al., 2019), while conventional reduced-order models can exhibit spurious behavior and accuracy degradation over extended time periods (Akhtar et al., 2009; Pant et al., 2021). Recent advances in physics-informed dynamic mode decomposition (piDMD) have demonstrated that embedding physical constraints into the model learning framework can improve long-term prediction stability (Baddoo et al., 2023). For gas–solid fluidized beds, where the pseudo-periodic nature of bubble dynamics is well-established, recurrence-based CFD provides an alternative pathway to computational acceleration by exploiting this inherent flow recurrence (Lichtenegger and Pirker, 2016).

Lichtenegger and Pirker (2016) introduced recurrence-based CFD (rCFD), a novel time-extrapolation methodology that exploits the pseudo-periodic nature of many industrial flows to achieve dramatic computational acceleration. The method leverages recurrence analysis proposed by Eckmann et al. (1995) to identify repeating flow patterns within a short monitoring period (τ_{rec}) of high-fidelity CFD–DEM simulation. Rather than continuing expensive flow field calculations, rCFD constructs physically consistent long-term flow evolution by stitching together recurring flow segments identified through recurrence matrices (Lichtenegger and Pirker, 2016; Lichtenegger et al., 2017). The methodology exists in two variants: flow-based rCFD, which reconstructs entire flow field sequences and solves transport equations (Lichtenegger et al., 2017; Kieckhefen et al., 2019; Lichtenegger et al., 2019), and transport-based rCFD, which focuses directly on scalar transport using Lagrangian memory shift operations (Pirker and Lichtenegger, 2018; Dabbagh et al., 2020; Pirker et al., 2025). Transport-based rCFD, employed in this work, translates continuous flow displacement into cell-to-cell memory shift patterns (Lumetzberger et al., 2025). These shift operations, governed by recurrence statistics, propagate scalar quantities such as species concentration or temperature without recalculating flow fields, achieving speed-ups of several orders of magnitude while maintaining accuracy comparable to full CFD–DEM simulations.

Transport-based rCFD has demonstrated agreement with full CFD–DEM simulations in preliminary studies (Pirker and Lichtenegger, 2018; Dabbagh et al., 2020; Pirker et al., 2025), suggesting potential for real-time process prediction and control. By reducing computational time from months to minutes, rCFD could enable real-time optimization of pharmaceutical coating uniformity, dynamic control of combustion efficiency, and predictive maintenance of industrial reactors. However, these applications demand rigorous validation of rCFD's ability to accurately extrapolate long-term behavior from short monitoring periods. While previous validations compared rCFD against CFD–DEM simulations, no study has validated time-extrapolated rCFD predictions against experimental measurements of internal flow dynamics over extended periods. This work addresses this critical gap using MRI to

validate both the underlying CFD–DEM model and long-term rCFD extrapolations.

This study provides comprehensive experimental validation of rCFD methodology through systematic comparison with MRI measurements. First, CFD–DEM simulations employing four drag models (Koch & Hill, Di Felice, Gidaspow, Beetstra) were validated against MRI data from a poppy seed fluidized bed operated at 1.5 u_{mf}. The validated CFD–DEM configuration was then used to generate a recurrence database for rCFD time extrapolation. Finally, time-extrapolated rCFD predictions over 10 s were compared against extended MRI measurements to assess long-term accuracy. This validation framework establishes rCFD as a reliable tool for process simulation and control.

2. Simulation

2.1. CFD-DEM model

CFD–DEM simulations were performed using the open-source framework CFDEMcoupling-PFM (Kloss et al., 2012; Department of Particulate Flow Modelling, Johannes Kepler University, 2024), which couples OpenFOAM v6.0 for fluid phase calculations with LIGGGHTS-PFM for particle dynamics. Comprehensive descriptions of the CFD–DEM methodology are available in previous reviews (Deen et al., 2007; Zhou et al., 2010); we present here the governing equations and modeling choices relevant to this study.

2.1.1. Gas phase

The gas phase is modeled using locally averaged Navier–Stokes equations. For a gas–solid system, the continuity and momentum equations governing gas flow with density ρ_g and velocity field $\mathbf{u}_g$ are:

$$\frac{\partial\left(\alpha_g\right)}{\partial t}+\nabla\cdot\left(\alpha_g\mathbf{u_g}\right)=0\ , \tag{1}$$

$$\frac{\partial}{\partial t}\left(\alpha_g\mathbf{u}_g\right)+\nabla\cdot\left(\alpha_g\mathbf{u}_g\mathbf{u}_g\right)=-\alpha_g\frac{\nabla p}{\rho_g}+\alpha_g\sum_{i=1}^{n}\frac{\mathbf{f}_{d,i}+\mathbf{f}_{ext,i}}{\rho_g\Delta V}+\frac{\alpha_g}{\rho_g}\nabla\cdot\left[\rho_g(\mu+\mu_t)\left(\nabla\mathbf{u}_g+\left(\nabla\mathbf{u}_g\right)^T\right)\right]\ . \tag{2}$$

where α_g represents the local gas void fraction, p is the pressure, μ is the dynamic viscosity, μ_t is the turbulent viscosity computed using the standard k-ε turbulence model (Launder and Spalding, 1983) within the Reynolds-Averaged Navier–Stokes (RANS) framework, and ΔV is the computational cell volume. In unresolved CFD–DEM simulations, $\alpha_g<1$ accounts for the volume occupied by particles within each cell. The momentum equation includes particle-related force terms: drag force ($\mathbf{f}_{d,i}$) and external forces ($\mathbf{f}_{ext,i}$) such as gravitational, electrostatic forces. The local void fraction for each cell is computed as follows:

$$\alpha_g=1-\frac{\sum_{i=1}^{n}V_{p,i}}{\Delta V}\ . \tag{3}$$

where $V_{p,i}$ is the volume of particle i located within the computational cell.

2.1.2. Solid phase

Particle motion in DEM is governed by Newton's second law. Particles are modeled as soft, deformable spheres using a spring-dashpot contact model, allowing controlled overlap that enables larger integration time steps. The translational and rotational equations of motion for particle i with mass m_i and moment of inertia I_i are:

$$m_i\dot{\mathbf{v}}_i=\mathbf{F}_i^{(p-p)}+\mathbf{F}_i^{(p-f)}+\mathbf{F}_i^{(\mathrm{ext})}\ , \tag{4}$$

$$I_i\dot{\boldsymbol{\omega}}_i=\boldsymbol{\tau}_i. \tag{5}$$

where $\mathbf{F}_i^{(p-p)}$ represents forces from particle–particle collisions, $\mathbf{F}_i^{(p-f)}$ represents fluid–particle interaction forces, $\mathbf{F}_i^{(\mathrm{ext})}$ represents external forces (gravity, electrostatic), and $\boldsymbol{\tau}_i$ is the net torque from tangential contact forces and rolling friction. The particle–particle interaction force is decomposed into normal and tangential components:

$$\mathbf{F}_i^{(p-p)}=\sum_{j\neq i}\left(\mathbf{F}^{(n)}\left(\mathbf{r}_i,\mathbf{v}_i,\boldsymbol{\omega}_i;\mathbf{r}_j,\mathbf{v}_j,\boldsymbol{\omega}_j\right)+\mathbf{F}^{(t)}(\mathbf{r}_i,\mathbf{v}_i,\boldsymbol{\omega}_i;\mathbf{r}_j,\mathbf{v}_j,\boldsymbol{\omega}_j)\right)\ . \tag{6}$$

where the sum extends over all particles j in contact with particle i. The normal force $\mathbf{F}^{(n)}$ and tangential force $\mathbf{F}^{(t)}$ depend on particle positions, translational velocities, and angular velocities. These forces are computed using the soft-sphere model of Cundall and Strack (Cundall and Strack, 1979), which represents contact mechanics through particle overlaps, relative velocities, and material properties: friction coefficient (μ), spring stiffnesses (k_n, k_t), and damping coefficients (c_n, c_t). Particle–wall contacts are treated analogously by assigning material properties to wall boundaries.

Rolling friction effects during particle collisions were modeled using the elastic–plastic spring-dashpot (EPSD) model, which accounts for energy dissipation during rolling motion.

The fluid–particle interaction force $\mathbf{F}_i^{(p-f)}$ comprises pressure gradient and drag contributions. To satisfy momentum conservation between phases:

$$\mathbf{F}_i^{(p-f)}=f_p-\frac{V_i}{1-\alpha_g(\mathbf{r}_i)}\mathbf{f}_{drag}(\mathbf{r}_i,\mathbf{v}_i)\ . \tag{7}$$

where f_p represents the pressure gradient force, calculated as follows:

$$f_p=-\frac{1}{6}\pi d_p^3\nabla p_g\ . \tag{8}$$

where d_p is particle diameter, particle drag forces depend on local void fraction and relative velocity between gas and particles. This work compares four drag correlations against MRI measurements: Hill et al. (2001), Di Felice (1994), Gidaspow (1994), and Beetstra et al. (2007). Each model expresses the drag force as:

$$\mathbf{f}_{drag}=\frac{1}{2}C_D\rho_gA'\left|u_g-v_p\right|\left(u_g-v_p\right)\ . \tag{9}$$

where ρ_g is the gas density, A' is the projected area of the particles in the flow field, C_D is the drag coefficient. Many scholars have proposed different correlations for C_D, which can be divided into two main categories: sparse particle systems and dense particle systems. The relationship between Re and C_D is closely interconnected, and establishing an accurate correlation is crucial for describing their variation.

Reynolds number is given as follows:

$$\mathrm{Re}=\frac{\rho_g|v_p-u_g|d_p}{\mu_g}\ . \tag{10}$$

In practical applications, complex flow regime changes must be considered. Engineering solutions typically rely on empirical formulations of the Reynolds number (Re) vs. C_D relationship. The drag coefficient exhibits characteristic behavior across different flow regimes (Zhao et al., 2023). In the laminar flow region, C_D shows a linear decrease with increasing Reynolds number. Subsequently, in the transition region, the rate of decrease is greatly reduced. Finally, in the turbulent region, C_D remains approximately constant at large Re values.

The drag force coefficient C_D depends on the drag model considered. This study focuses on the empirical correlations shown in Table 1.

The four drag models evaluated in this study represent different approaches to capturing fluid–particle interactions in dense gas–solid flows. The Koch & Hill model (Hill et al., 2001) is derived from direct numerical simulations and explicitly accounts for particle clustering and hydrodynamic interactions in dense flows, predicting higher drag forces in regions with significant particle aggregation (Han et al., 2024; Guo et al., 2021). The Di Felice model (Di Felice, 1994) introduces a void fraction-dependent exponent to the single-particle drag coefficient, providing improved accuracy for high solid concentration regimes and yielding better agreement with experimental velocity profiles in dense fluidized beds (Agrawal et al., 2018; Wang et al., 2021). The Gidaspow

Table 1
Drag coefficient correlations for dense particle systems.

Reference	Drag coefficient equation
Hill et al. (2001)	$C_D = \frac{4}{3}\left(\frac{\alpha_s(1-\alpha_g)A(\alpha_g)}{\alpha_g \mathrm{Re}} + \alpha_g B(\alpha_g)\right)$ where $A(\alpha_g) = \begin{cases} \frac{18\alpha_g^3}{(1-\alpha_g)}\left[1+\frac{3}{2}\sqrt{1-\alpha_g}+\frac{135}{64}(1-\alpha_g)\ln(1-\alpha_g)+17.14(1-\alpha_g)\right] \\ \quad \times\left[1+0.681(1-\alpha_g)-8.48(1-\alpha_g)^2+8.16(1-\alpha_g)^3\right]^{-1} \\ \quad \text{for } \alpha_g \geq 0.6 \\ 180 \quad \text{for } \alpha_g < 0.6 \end{cases}$ $B(\alpha_g) = 0.6057(1-\alpha_g)^2 + 1.908(1-\alpha_g)\alpha_g^2 + \frac{0.209}{\alpha_g^3}$
Di Felice (1994)	$C_D = \left(0.63 + \frac{4.8}{\sqrt{\alpha_g \mathrm{Re}}}\right)^2 \alpha_g^{2-\zeta}$ where $\zeta = 3.7 - 0.65\exp\left[-\frac{(1.5-\log(\alpha_g \mathrm{Re}))^2}{2}\right]$
Gidaspow (1994)	$C_D = \begin{cases} \frac{24}{\alpha_g \mathrm{Re}}\left[1+0.15(\alpha_g \mathrm{Re})^{0.687}\right]\alpha_g^{-1.65} & \alpha_g > 0.8; \alpha_g \mathrm{Re} < 1000 \\ 0.44\alpha_g^{-1.65} & \alpha_g > 0.8; \alpha_g \mathrm{Re} \geq 1000 \\ 200\frac{1-\alpha_g}{\alpha_g \mathrm{Re}} + \frac{7}{3} & \alpha_g \leq 0.8 \end{cases}$
Beetstra et al. (2007)	$C_D = \frac{4}{3}\left[180\frac{1-\alpha_g}{\alpha_g \mathrm{Re}} + 18\frac{\alpha_g^4(1+1.5\sqrt{1-\alpha_g})}{\alpha_g \mathrm{Re}} + 0.31\frac{\alpha_g^{-1}+3(1-\alpha_g)\alpha_g+8.4(\alpha_g \mathrm{Re})^{-0.343}}{1+10^{3(1-\alpha_g)}(\alpha_g \mathrm{Re})^{-0.5-2(1-\alpha_g)}}\right]$

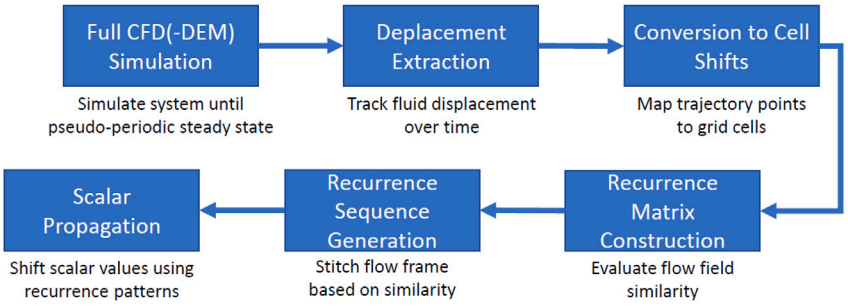

Fig. 1. Transport-based rCFD methodology workflow.

model (Gidaspow, 1994) combines the Wen–Yu correlation for dilute regimes ($\varepsilon_g > 0.8$) with the Ergun equation for dense regimes ($\varepsilon_g \leq 0.8$), offering broad applicability across varying solid volume fractions and widespread use in CFD–DEM simulations of spouted and bubbling beds (Zhou et al., 2017; Che et al., 2023). The Beetstra model (Beetstra et al., 2007), developed from Lattice-Boltzmann simulations of random sphere arrays, provides a detailed hydrodynamic interaction representation suitable for intermediate to dense particle concentrations, often predicting higher drag forces in dense regions and demonstrating good performance at low gas velocities (Marchelli et al., 2020; Atxutegi et al., 2021).

2.2. Data-driven recurrence based CFD (rCFD)

The pseudo-repetitive nature of the flow behavior in fluidized bed flow enables time extrapolation using recurrence statistics concepts, including recurrence plots and signal reconstruction. Implementation details for transport-based rCFD are provided by Pirker and Lichtenegger (Pirker and Lichtenegger, 2018). Fig. 1 illustrates the transport-based rCFD workflow employed in this study.

The following subsections summarize the key aspects of rCFD methodology relevant to this study.

2.2.1. Recurrence statistics

Recurrence plots are constructed from the gas void fraction field throughout the computational domain (Lichtenegger et al., 2017). The recurrence plot quantifies similarity between flow states at different time steps through a correlation matrix calculated as:

$$R_{\alpha_g}(t_i, t_j) = \frac{1}{N_{\alpha_g}} \int_V (\alpha_g(t_i) - \alpha_g(t_j))^2 \, dV, \tag{11}$$

$$N_{\alpha_g} = \max_{t_i, t_j} \int_V (\alpha_g(t_i) - \alpha_g(t_j))^2 \, dV. \tag{12}$$

where t_i and t_j represent two time instances with corresponding flow states, V is the entire flow domain, and N_{α_g} is a normalization factor. The normalization ensures that identical flow states (main diagonal) have $R_{\alpha_g} = 0$, while maximally dissimilar states approach $R_{\alpha_g} = 1$.

The temporal resolution for recurrence pattern reconstruction must satisfy:

$$\Delta t_{rec} < \sqrt{\frac{\langle \gamma^2 \rangle}{\langle (\partial\gamma/\partial t)^2 \rangle}}. \tag{13}$$

where γ is the field quantity of interest (gas void fraction), and $\langle \cdot \rangle$ denotes time averaging. The rCFD time step must be smaller than Δt_{rec} to adequately resolve recurrent flow patterns.

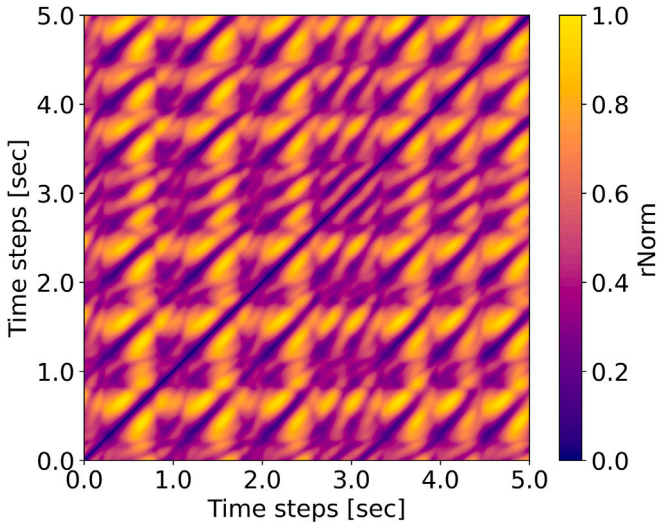

Fig. 2. Recurrence distance plot comparing the time steps from full CFD–DEM input data. A value of zero indicates almost similar flow state and a value of 1 indicates dissimilar flow states. (For interpretation of the references to color in this figure legend, the reader is referred to the web version of this article.)

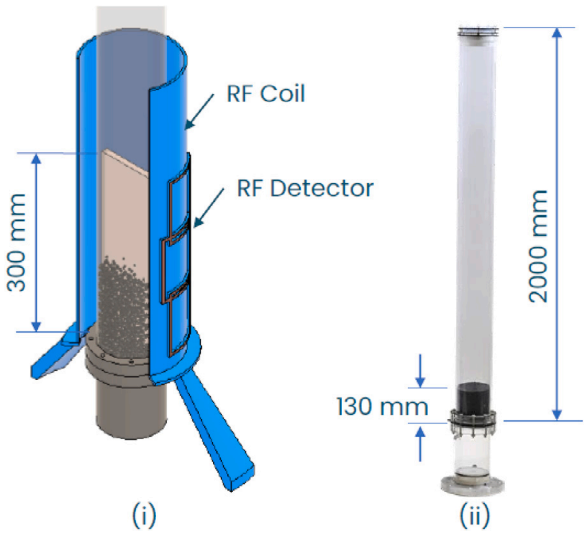

Fig. 3. (i) Sketch of RF coil and detector around 3T MRI, and mid-plane considered for solid fraction imaging (ii) Acrylic fluidized bed setup used in MRI.

2.2.2. Recurrence processes

Based on the recurrence plot as shown in Fig. 2, time indices are compared, most similar time indices are stitched one after another, leading to a time extrapolation process. The recurrence distance matrix exhibits characteristic banded structure: the main diagonal (zero distance, identical states) and parallel bands indicating flow states separated by approximately τ_{rec}. Low-distance regions (dark blue) represent recurring flow patterns, while high-distance regions (bright yellow) indicate dissimilar states during the transition between bubble formation and coalescence events. This structure confirms the pseudo-periodic behavior enabling rCFD extrapolation.

The identified recurrence patterns provide the foundation for transport-based rCFD extrapolation, which reconstructs long-term scalar transport (e.g., species concentration, temperature) by intelligently sequencing similar flow segments without resolving momentum equations.

3. Materials and methods

3.1. Experimental setup

Experiments were conducted in an MRI-compatible fluidized bed with an outer diameter of 100 mm and an inner diameter of 96 mm. The fluidized bed was open to the atmosphere, but the top was covered with a filter to prevent particle elutriation. Pressurized air was used as the fluidizing gas, and its volumetric flow rate was controlled using a mass flow controller (F-202AV, Bronkhorst), at 1.5 times the minimum fluidization velocity (u_{mf}). The u_{mf} was determined by measuring the pressure drop across the particle bed at decreasing air velocities. Air is uniformly distributed to the particle bed through a sintered porous plate with a pore size of 20 μm and a thickness of 5 mm. The fluidized bed was filled with poppy seeds to a height of 130 mm, and the particles are classified as Geldart group D.

Bubble properties were investigated using a 3 T Magnetic Resonance Imaging (MRI) system. A birdcage radiofrequency (RF) coil of the imaging system was used to excite the particles, while the signals were detected by a custom-built 15-channel RF detector array as shown in Fig. 3. The oil contained within the poppy seeds generates the MRI signal, consequently, bubbles could be identified from the resulting images based on intensity differences. A cylindrical RF coil was placed around the fluidized bed to enhance the signal-to-noise ratio in the acquired images. The use of multichannel coils enables parallel imaging, wherein the spatial sensitivity of each coil element is used as additional information in the image reconstruction process. This approach reduces the number of data points that must be sampled, thereby increasing the temporal resolution and allowing the detection of bubble dynamics. In the experiments, the temporal resolution was 20 ms, and the spatial resolution was 4 mm by 8 mm. The field of view was selected to fully capture the expanded bed during operation. Particle signal intensities in a vertical slice (of 10 mm thickness) through the center of the bed were averaged, and 500 consecutive frames were acquired using a fast field echo pulse sequence at each volumetric flow rate during the experiments.

Acquired images were processed using OpenCV with Python to segment bubbles. Threshold based image segmentation enabled the detection of bubbles, where the high signal intensity in the frames corresponded to the particles, while the low signal intensity indicated the bubbles. Subsequently, morphological operations such as dilation were applied to expand the bubble regions, and erosion was used to smooth the bubble edges. The equivalent bubble diameter was then calculated based on the area of the pixels representing the bubbles.

3.2. Simulation setup

The CFD–DEM computational domain replicated the experimental fluidized bed geometry (Fig. 4) with an internal diameter of 96 mm. The domain height was reduced to 600 mm compared to the experimental apparatus height of 2000 mm, since maximum bed expansion remained below 250 mm for the superficial velocity under investigation. This truncation reduces computational cell count near the outlet without affecting bed dynamics.

Gas phase boundary conditions matched experimental operating conditions. A uniform velocity inlet was imposed at the domain bottom, simplifying the complex sintered distributor plate geometry while preserving essential gas distribution physics. This approach is standard practice for gas–solid fluidized bed simulations (Sasic et al., 2006; Kanholy and Battaglia, 2012). The outlet was set to atmospheric pressure with zero-gradient velocity, and walls employed no-slip conditions.

Table 2
CFD–DEM mesh configuration and numerical parameters.

CFD mesh	
Mesh type	Modified Butterfly Grid (SC)
Number of mesh cells, N_{cells}	268,800
Discretizations	
Diameter ($\Delta X_{cells}, Z_{cells}$)	28
Bed Height (ΔY_{cells})	200
Cell sizes	
$\Delta X_{cells}, Z_{cells}$	≈3 mm [≈2.75 d_p]
Bed Height, ΔY_{cells}	≈3 mm [≈2.75 d_p]
CFD–DEM simulation	
CFD time step, Δt_{CFD} (s)	5×10^{-5}
Maximum Courant number, $Co_{max,CFD}$	1
CFD write interval, $\Delta t_{W,CFD}$ (s)	5×10^{-3}
DEM time step, Δt_{DEM} (s)	2.5×10^{-6}
Number of particles, N_{DEM}	$\approx 1 \times 10^{6}$
Recurrence CFD simulation	
Global time step, Δt_{CFD} (s)	5×10^{-3}
Particle Courant number, $Co_{max,P,CFD}$	1

Table 3
Material properties and contact parameters for poppy seeds and apparatus walls.

Particle size distribution		
Diameter, $d_{p_i,32}$ (mm)		1.16
d_{p_1} (mm)		0.919 (35%)
d_{p_2} (mm)		1.050 (32%)
d_{p_3} (mm)		1.269 (33%)
Poppy Seeds Properties		
Particle density, ρ_P (kg/m^3)		1015
Young's modulus, $Y_P = Y_W$ (Pa)		1×10^7
Poisson's ratio, $s_P = s_W$		0.3
Coefficient of restitution	e_{P-P}	0.899
	e_{P-W}	0.772
Coefficient of friction	$k_{fr,P-P}$	0.134
	$k_{fr,P-W}$	0.870
Coefficient of rolling friction	$k_{fr,P-P}$	0.844
	$k_{fr,P-W}$	0.581

3.3. Data extraction and post-processing methods

3.3.1. CFD-DEM data extraction pipeline

CFD–DEM simulations were performed for all operating conditions using the numerical parameters mentioned in Tables 2 and 3. Simulation data extraction followed a systematic seven-step pipeline designed to enable quantitative comparison between CFD–DEM predictions and MRI measurements.

Step 1: CFD-DEM Simulation Execution

All simulations were run until a statistical steady-state was achieved, typically requiring 5 s of physical time to eliminate initial transient effects. The solid volume fraction field was recorded at 200 Hz temporal resolution, while the experimental MRI acquisition frequency was 50 Hz.

Step 2: Mid-Plane Data Extraction

Using the ParaView post-processing tool, the solid volume fraction (α_s) was extracted at the mid-plane ($z = 0$, Fig. 4) for all time steps. This 2D slice corresponds to the MRI measurement plane and reduces 3D simulation data to a format directly comparable with experimental images.

3.3.2. Binary thresholding and frame generation

Step 3: MRI Binary Thresholding

MRI experimental frames were converted to binary format using intensity-based thresholding as described in Section 3.1. Binary conversion distinguished between gas-rich regions (voids/bubbles) and solid-rich regions (particle emulsion phase).

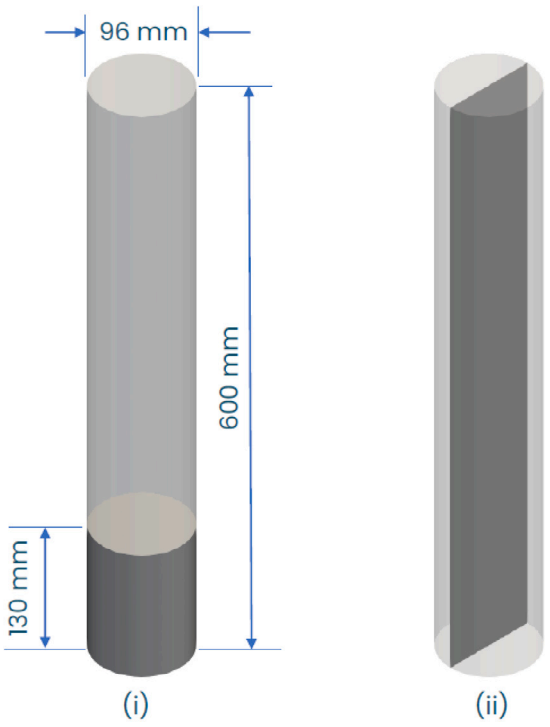

Fig. 4. (i) Computational domain with static bed height of 130 mm. (ii) Mid-plane location ($z = 0$) extracted for comparison with MRI measurements.

Step 4: CFD-DEM Frame Extraction

Solid volume fraction fields from CFD–DEM simulations were processed to generate binary frames using multiple threshold values: $\alpha_s = 0.15, 0.20, 0.25, 0.30, 0.35$, and 0.40. For each threshold value, binary frames were generated according to:

$$B(x,y,t) = \begin{cases} 0 & \text{if } \alpha_s(x,y,t) < \alpha_{s,\text{threshold}} \text{ (gas-rich region)} \\ 1 & \text{if } \alpha_s(x,y,t) \geq \alpha_{s,\text{threshold}} \text{ (solid-rich region)} \end{cases} \quad (14)$$

This multi-threshold approach enables systematic analysis of sensitivity to the gas–solid interface definition and optimization of the threshold value for each metric.

3.3.3. Optimal threshold analysis framework

Step 5: Multiple Threshold Processing

The optimal solid volume fraction threshold for each metric was determined using a multi-criteria analysis framework addressing the challenge that different physical metrics may be optimally captured at different threshold values. Evaluation criteria included: (1) statistical robustness (low coefficient of variation), (2) measurement precision (signal-to-noise ratio optimization), and (3) experimental validation (compatibility with MRI contrast characteristics).

Step 6: Optimal Threshold Selection

For each threshold and metric combination, uncertainty was quantified using bootstrap resampling with 10,000 iterations. For each threshold $\alpha_{s,i}$, the bootstrap procedure sampled with replacement from the metric data, calculated mean and median statistics, and determined 95% confidence intervals as the 2.5th and 97.5th percentiles of the bootstrap distribution. Coefficient of variation was computed as CV = $\sigma/\mu \times 100\%$.

Distribution differences between threshold groups were assessed using the Kolmogorov–Smirnov test:

$$D_{KS} = \max_x |F_1(x) - F_2(x)| \ . \quad (15)$$

where $F_1(x)$ and $F_2(x)$ are cumulative distribution functions for different threshold conditions.

Sensitivity gradient analysis

The sensitivity of each metric to threshold selection was quantified using finite difference approximation:

$$S = \frac{\partial M}{\partial \alpha_s} \approx \frac{M_{i+1} - M_i}{\alpha_{s,i+1} - \alpha_{s,i}} . \tag{16}$$

where M represents the metric of interest. Optimal thresholds exhibit moderate sensitivity gradients, avoiding excessive instability (high $|S|$) or insufficient responsiveness (low $|S|$).

3.3.4. Bubble detection and characterization

Step 7: Final Post-Processing with Optimal Threshold

Using the optimal threshold value determined from Step 6, final post-processing was performed to calculate all metrics of interest, including bubble characteristics, bed expansion statistics, and radial distribution profiles.

Bubble identification employed OpenCV contour detection algorithms applied to binary frames. The detection algorithm consisted of four steps: (1) contour extraction using `cv2.findContours()` with `RETR_EXTERNAL` mode, (2) area filtering with minimum bubble area of 4 mm^2, (3) boundary exclusion to remove artifacts near the free surface and inlet, and (4) geometric analysis to calculate equivalent diameter, aspect ratio, and centroid position.

Equivalent bubble diameter and aspect ratio were calculated as:

$$D_{\text{eq}} = 2\sqrt{\frac{A}{\pi}} , \tag{17}$$

$$\text{AR} = \frac{w}{h} . \tag{18}$$

where A is the bubble area (mm^2), w is the bubble width, and h is the bubble height based on minimum bounding rectangle.

Bubble velocities were calculated using nearest-neighbor tracking between consecutive frames. For each bubble centroid at time t, the nearest bubble centroid at time $t + \Delta t$ within a maximum displacement threshold was identified. Velocity components were computed as:

$$v_x = \frac{\Delta x}{\Delta t}, \quad v_y = \frac{\Delta y}{\Delta t} , \tag{19}$$

$$|v| = \sqrt{v_x^2 + v_y^2} . \tag{20}$$

where Δx and Δy are horizontal and vertical displacements, respectively.

A minimum track length of two frames was required, corresponding to minimum residence time of 40 ms and minimum displacement of 20 mm. This criterion was selected based on expected bubble velocities of 5–80 cm/s for the experimental system (Pigford, 1968).

3.3.5. Bed expansion analysis

Bed expansion was quantified through automated free surface detection. For each binary frame, the particle occupancy fraction was calculated for each horizontal row. The free surface was defined as the top most row with particle occupancy exceeding 10%, representing the transition from particle-laden bed to freeboard region.

Bed expansion height was calculated from the free surface pixel location using the image spatial resolution:

$$H_{\text{expansion}} = y_{\text{surface}} \cdot r_y , \tag{21}$$

where y_{surface} is the free surface pixel coordinate and r_y is the spatial resolution (mm/pixel). The expansion ratio relative to static bed height ($H_{\text{static}} = 130$ mm) was:

$$R_{\text{expansion}} = \frac{H_{\text{expansion}}}{H_{\text{static}}} . \tag{22}$$

Temporal statistics were calculated over all frames:

$$\mu_H = \frac{1}{n}\sum_{i=1}^{n} H_i , \tag{23}$$

$$H_{\max} = \max(H_i) , \tag{24}$$

$$\sigma_H = \sqrt{\frac{1}{n-1}\sum_{i=1}^{n}(H_i - \mu_H)^2} . \tag{25}$$

where n is the total number of frames. Bootstrap resampling with 10,000 iterations provided uncertainty quantification for all temporal statistics.

3.3.6. Radial distribution analysis

Radial particle distributions were quantified using two approaches. In full-bed analysis, particle presence was averaged over the entire instantaneous bed height to capture overall radial segregation patterns. In static-bed analysis, only the region below the static bed height ($H_{\text{static}} = 130$ mm) was considered, focusing on the dense phase radial distribution. For each radial position r, the time-averaged solid fraction was computed as:

$$\langle \alpha_s(r) \rangle = \frac{1}{n_t n_y}\sum_{t=1}^{n_t}\sum_{y=1}^{n_y} \alpha_s(r, y, t) . \tag{26}$$

where n_t is the number of time steps and n_y is the number of vertical positions within the analysis region.

3.3.7. Statistical quality criteria

Statistical quality indicators for threshold acceptance included: coefficient of variation below 30%, bootstrap confidence interval widths less than 30% of the mean value, KS test p-values greater than 0.01, gradient quality scores above 0.3, and physically realistic bubble velocities within the expected range of 5–80 cm/s for the experimental system (Pigford, 1968). Thresholds failing these criteria were excluded from analysis.

This comprehensive post-processing framework provides reproducible, statistically robust analysis for quantitative validation of CFD–DEM predictions against MRI measurements. The multi-threshold optimization approach addresses the fundamental challenge of defining gas–solid interfaces in computational simulations while maintaining physical realism and statistical rigor.

4. Results and discussion

4.1. Drag model selection

Selection of an appropriate drag correlation is crucial for accurately capturing fluidized bed dynamics. While numerous studies have reviewed drag model selection (Kloss et al., 2012; Zhao et al., 2024; Golshan et al., 2020; Kieckhefen et al., 2020), most validations rely on theoretical correlations or intrusive experimental measurements that disturb natural flow behavior. This study validates four drag models Koch & Hill, Di Felice, Gidaspow, and Beetstra against non-invasive MRI measurements of mid-plane flow dynamics. Validation metrics include bed expansion behavior, mean bed height, bubble size distributions, bubble velocity statistics, and radial particle distribution profiles.

Table 4 shows the optimal solid fraction thresholds used for binary frame conversion in each validation metric for the four drag models. All analyses throughout this study apply these optimized threshold values. The multi-criteria threshold selection procedure is detailed in Section 3.3.

Fig. 5 compare bed expansion dynamics at 1.5 u_{mf} for all drag models against MRI measurements. All models predict mean bed heights within ±1 cm of the experimental value, demonstrating reasonable quantitative agreement. However, temporal dynamics reveal important differences. The Di Felice model predicts a mean bed height of 16.5 cm, close to the MRI value of 16.8 cm (Fig. 6), but fails to capture the amplitude and frequency of primary expansion peaks (Fig. 5). The Gidaspow and Beetstra models overpredict mean bed height at 17.5 cm

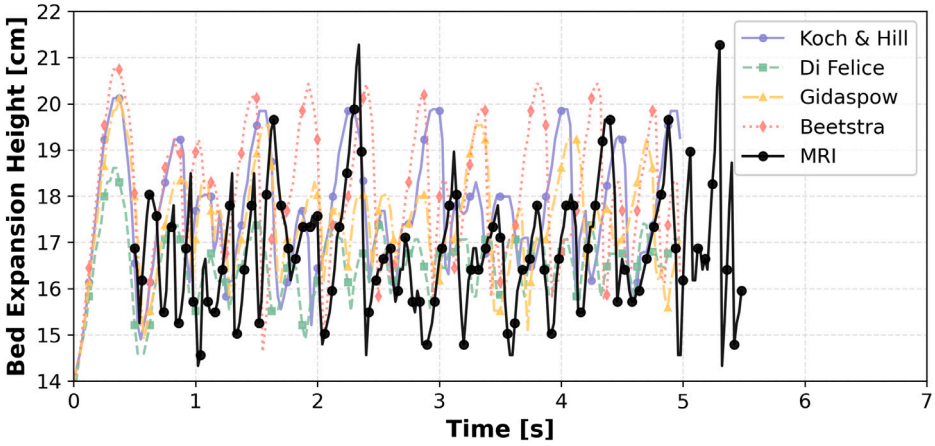

Fig. 5. Mean bed height over time across all drag models and MRI data for inlet velocity of 0.45 m/s (1.5 u_{mf}).

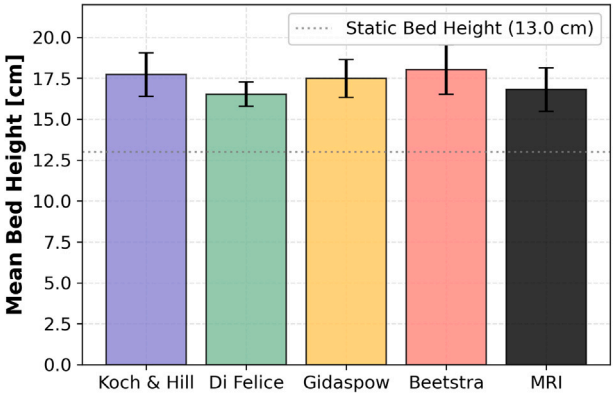

Fig. 6. CFD–DEM simulation with different drag models and MRI data for inlet velocity of 0.45 m/s (1.5 u_{mf}).

Table 4
Comparison of mean solid fraction (α_s) considered for binarization of each frame for different drag models at 1.5 U_{mf} based on optimal threshold analysis (Section 3.3.3).

Metric	Koch & Hill	Di Felice	Gidaspow	Beetstra
Mean bed expansion	0.198	0.285	0.208	0.211
Mean bubble velocity	0.285	0.198	0.285	0.285
Mean bubble diameter	0.330	0.285	0.285	0.144
Mean radial distribution	0.329	0.329	0.329	0.329

and 18.0 cm, respectively. The Beetstra model additionally fails to reproduce secondary expansion peaks with correct frequency, while the Gidaspow model shows inconsistent peak timing and amplitude compared to MRI measurements.

The Koch & Hill model predicts a mean bed height of 17.7 cm, an overprediction of 0.9 cm. Despite this offset, the model accurately reproduces both the amplitude and frequency of primary and secondary expansion peaks, achieving excellent qualitative and quantitative agreement with MRI temporal dynamics (Fig. 5).

Measurement of internal bubble size distributions without flow disturbance remains a critical validation challenge (Jiang et al., 2024; Liu et al., 2010; Okhovat-Alavian et al., 2020). MRI provides non-invasive access to these data, enabling direct comparison with CFD–DEM predictions. Fig. 7(a) reveals a systematic deficiency across all drag models: bubbles smaller than 7.5 mm are absent in simulations but clearly present in MRI measurements. These small bubbles form predominantly near the distributor plate (Fig. 7(b)), suggesting that the uniform velocity inlet boundary condition fails to capture initial bubble formation dynamics. While a more sophisticated distributor model (e.g., resolved porous media) may address this limitation.

All models underpredict maximum bubble diameter compared to the MRI-observed value of 75 mm (Fig. 7(a)). Predicted maxima are: Di Felice (40 mm), Gidaspow (55 mm), Koch & Hill (62.5 mm), and Beetstra (67.5 mm). A general trend of decreasing bubble velocity with increasing diameter is observed across all models except Gidaspow, which exhibits anomalously high velocities (exceeding 40 cm/s) for bubbles in the 45–50 mm size range. This unphysical behavior, combined with underprediction of maximum bubble size, suggests the Gidaspow model inadequately represents bubble dynamics in this system. Based on bubble velocity statistics, the Koch & Hill and Beetstra models demonstrate superior performance.

Fig. 7(b) presents average bubble diameter as a function of height above the distributor. While all models fail to predict small bubbles near the distributor (as discussed above), the Koch & Hill model achieves excellent agreement with MRI measurements throughout the upper bed region. Bubble growth rates and absolute diameters match experimental observations both qualitatively and quantitatively, supporting its selection for subsequent analyses.

Radial particle distribution profiles (Fig. 8) provide further discrimination among drag models. MRI measurements reveal relatively uniform particle distribution across the bed diameter (Fig. 8(a)), indicating that bubbles form preferentially near the walls rather than the centerline. The Koch & Hill model reproduces this behavior to a certain extent but not completely; the Di Felice model shows almost flat radial profiles with lower magnitudes particle presence intensity. In contrast, Gidaspow and Beetstra models predict U-shaped radial profiles with particle accumulation near walls and depletion at the centerline, indicating central bubble formation inconsistent with MRI evidence (Fig. 8(b)). This fundamental difference in predicted flow structure further supports the selection of the Koch & Hill drag model.

Table 5 provides an overview of the comparison study and the Koch & Hill drag model outperforms alternatives across multiple validation metrics: temporal bed expansion dynamics, bubble size distributions throughout the bed height, bubble velocity statistics, and radial particle distribution profiles. Despite this superior performance, all models fail to predict small bubble formation near the distributor plate. This systematic deficiency likely stems from the simplified uniform velocity inlet boundary condition, which cannot capture local gas jetting and initial bubble nucleation from a porous distributor. Resolution of this limitation requires either resolved porous media modeling or empirical inlet conditions calibrated to match near-distributor dynamics.

4.2. Effect of inlet boundary condition

The systematic absence of small bubbles near the distributor across all drag models (Section 4.1) motivated investigation of inlet boundary

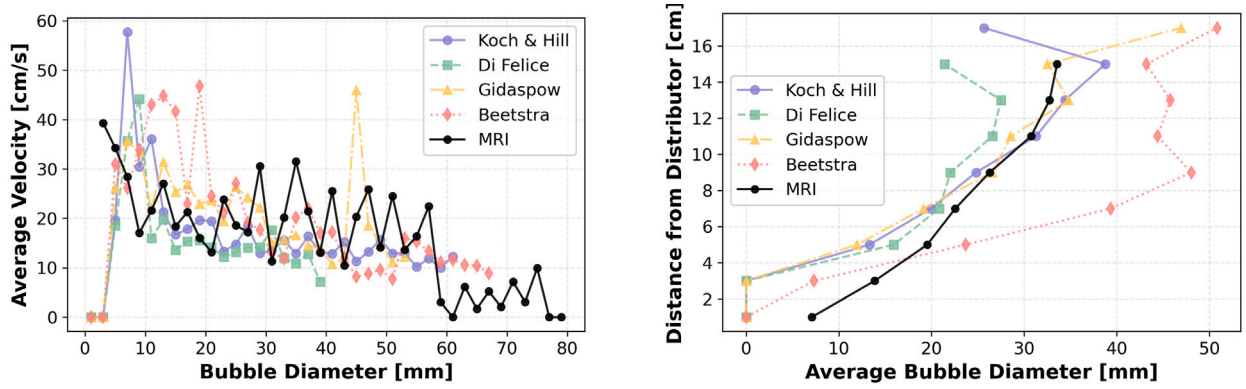

(a) Average bubble velocity of each bubble size class

(b) Average bubble diameter vs height of fluidized bed

Fig. 7. CFD–DEM simulation data with different drag models and MRI data for inlet velocity of 0.45 m/s (1.5 u_{mf}).

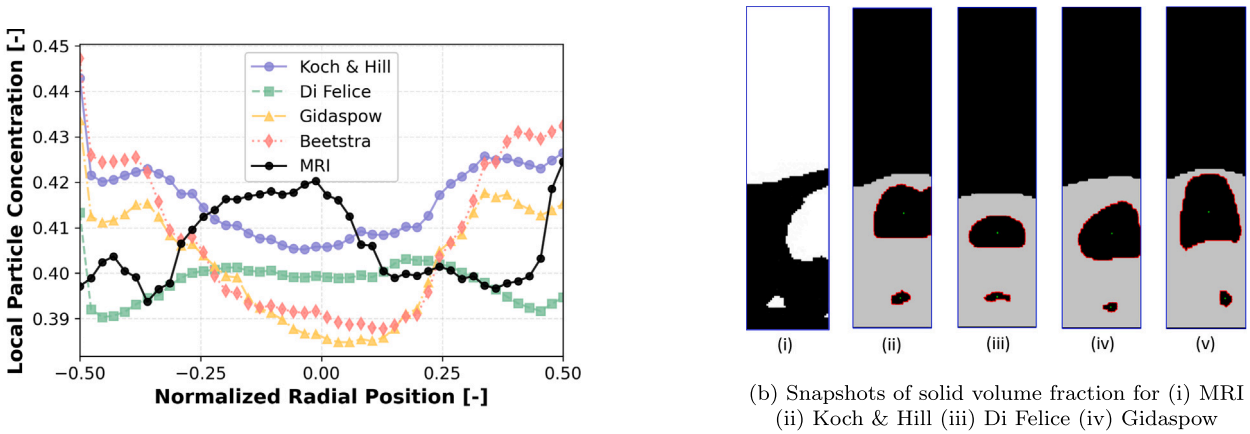

(a) Radial particle concentration distribution

(b) Snapshots of solid volume fraction for (i) MRI (ii) Koch & Hill (iii) Di Felice (iv) Gidaspow (v) Beetstra

Fig. 8. CFD–DEM simulation data with different drag models and MRI data for inlet velocity of 0.45 m/s (1.5 u_{mf}).

Table 5
Summary comparison of drag models against MRI measurements at 1.5 u_{mf}. MRI reference values: mean bed height = 16.8 cm, maximum bubble diameter = 75 mm.

Metric	Koch & Hill	Di Felice	Gidaspow	Beetstra
Mean bed height (cm)	17.7	16.5	17.5	18.0
Deviation from MRI (%)	+5.4	−1.8	+4.2	+7.1
Bed expansion dynamics	++	–	+	–
Maximum bubble diameter (mm)	62.5	40	55	67.5
Bubble diameter vs. height	++	+	++	–
Bubble velocity trend	+	–	–	+
Radial particle distribution	++	–	+	+
Small bubbles near distributor	No	No	No	No
Overall assessment	**Best**	Moderate	Moderate	Moderate

Qualitative ratings: ++ good agreement, + acceptable agreement, - poor agreement.

condition effects. Two OpenFOAM boundary conditions were compared using the Koch & Hill drag model with otherwise identical simulation parameters: *uniformFixedValue*, which imposes a spatially uniform inlet velocity, and *consistentSuperficialVelocityInlet*, which accounts for local void fraction by computing actual velocity as the specified superficial velocity divided by local porosity. The latter is physically more appropriate for porous distributor plates, as it couples inlet velocity to the local particle distribution.

The *consistentSuperficialVelocityInlet* boundary condition produced minimal differences compared to *uniformFixedValue*. Small bubbles near the distributor remained absent, although slightly larger bubbles (10–15 mm diameter) were predicted at 20 mm height compared to both MRI and the uniform inlet case (Fig. 9(a)). Radial particle distributions were nearly identical for both boundary conditions (Fig. 9(b)).

This constitutes a key finding of the present study: void fraction corrected inlet velocities alone cannot resolve, the near distributor bubble formation discrepancy, underscoring the inherent complexity of the distributor region where bubble nucleation is governed by discrete gas jetting rather than continuum level void fraction effects. Future work should explore spatially resolved inlet conditions derived from dedicated distributor region simulations or empirical measurements of jet penetration and bubble nucleation characteristics.

4.3. Recurrence statistics

CFD–DEM simulation data from the modified butterfly grid (SC mesh, 3 mm cell size) with the Koch & Hill drag model and uniform velocity inlet boundary condition were used as input for rCFD time extrapolation at 1.5 u_{mf}.

The rCFD framework requires input data spanning 3 to 4 characteristic recurrence periods (τ_{rec}). To determine τ_{rec} and the minimum required time step, Fast Fourier Transform (FFT) analysis was performed on the void fraction field at a representative mid-plane location (Fig. 10).

FFT analysis (Fig. 10(b)) reveals dominant frequencies corresponding to bubble formation and bed expansion cycles. The characteristic recurrence period is $\tau_{rec} \approx 0.27$ s, and the minimum time step for

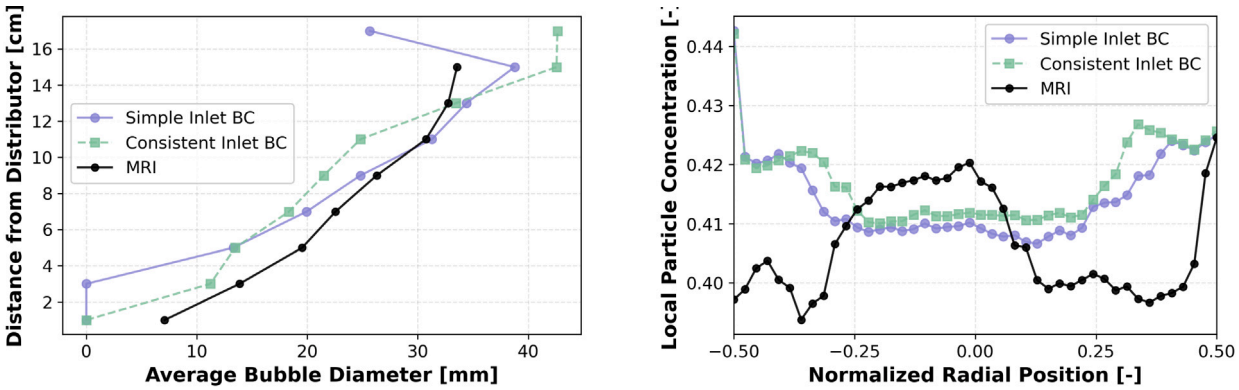

(a) Average bubble diameter over height (b) Radial particle concentration distribution

Fig. 9. Comparison of inlet boundary conditions for Koch & Hill drag model at 1.5 u_{mf}: (a) average bubble diameter versus height, (b) radial particle distribution. Both boundary conditions compared against MRI measurements.

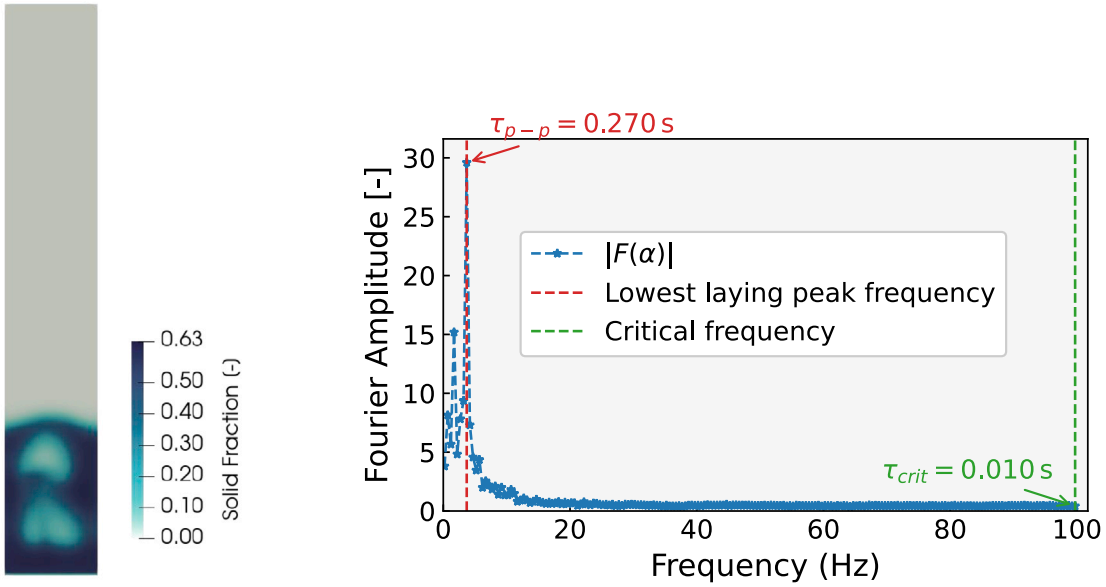

(a) 2D Plane for FFT analysis (b) FFT applied on a plane as shown in Figure 10a

Fig. 10. (a) Mid-section plane showing solid fraction in computational domain from Fig. 4 at $t = 1.4$ s. (b) FFT analysis reveals the recurrence period (τ_{p-p}) and minimum time step required for rCFD (τ_{crit}).

rCFD reconstruction is $\Delta t_{rec} = 0.01$ s, satisfying the temporal resolution criterion (Eq. (13)).

CFD–DEM simulations were executed for 5 s of physical time with data output at 200 Hz, generating 1000 flow field snapshots. The recurrence distance matrix (Fig. 2) quantifies pairwise similarity between all time steps using the void fraction field correlation metric (Eq. (11)).

4.4. rCFD time extrapolation

Five seconds of CFD–DEM input data (simulation details in Section 4.3) were used to extrapolate flow behavior to 10 s using transport-based rCFD. Mean bed height evolution exhibits excellent agreement between rCFD predictions and MRI measurements (Figs. 11 and 12(d)), validating the time extrapolation methodology.

Average bubble diameter profiles versus height (Fig. 12(a)) demonstrate that rCFD accurately reproduces trends observed in MRI data throughout the extrapolated 10 s period. As expected, small bubbles near the distributor remain absent in rCFD predictions, since this deficiency originates in the input CFD–DEM simulations (Section 4.1). Similarly, bubble velocity statistics as a function of diameter (Fig. 12(b)) show good agreement with MRI measurements, with rCFD maintaining the physical trend of decreasing velocity with increasing bubble size.

Radial particle distribution profiles (Fig. 12(b)) confirm that rCFD preserves the flow structure characteristics of the input CFD–DEM data. The relatively uniform radial distribution matches MRI observations, though with slightly reduced near-wall particle concentration compared to experiments. Overall, time-extrapolated rCFD results maintain fidelity to both the input CFD–DEM simulations and MRI measurements across all validation metrics, including temporal bed expansion dynamics, bubble size distributions, bubble velocity statistics, and radial segregation patterns.

As noted in Section 2.2, transport-based rCFD reconstructs scalar field evolution without resolving individual particle trajectories. The method operates at the continuum scale, tracking gas–solid interface motion through memory shift operations on the void fraction field. Consequently, instantaneous point-by-point comparison with CFD–DEM is

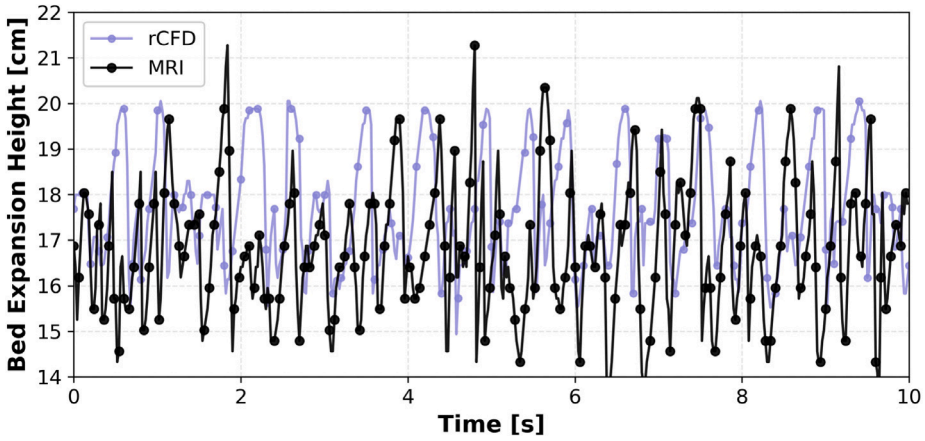

Fig. 11. Mean bed height over time rCFD vs. MRI for inlet velocity of 0.45 m/s (1.5 u_{mf}).

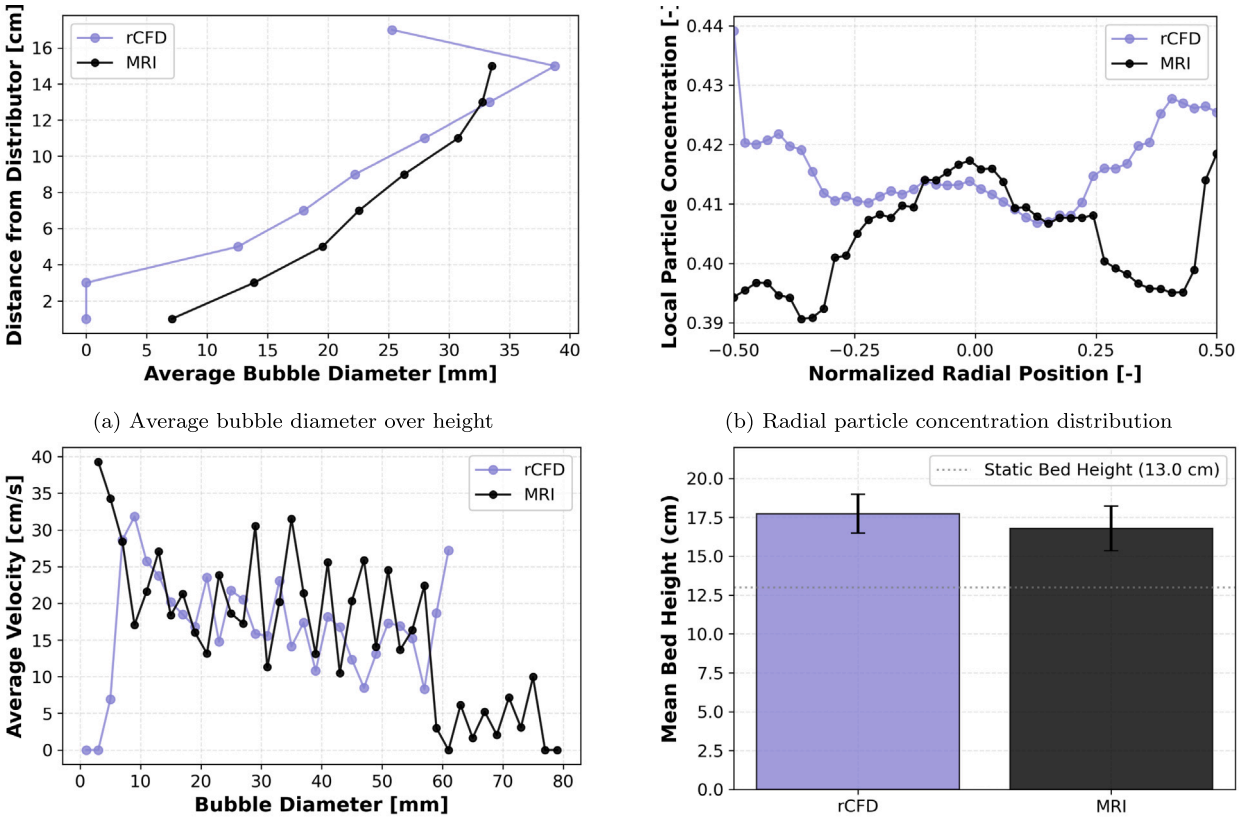

(a) Average bubble diameter over height

(b) Radial particle concentration distribution

(c) Average velocity of each bubble size class

(d) Overall mean bed height statistics

Fig. 12. rCFD vs. MRI data for inlet velocity of 0.45 m/s (1.5 u_{mf}).

not meaningful; instead, statistical validation of time-averaged quantities and distribution functions provides appropriate verification.

The computational efficiency of rCFD enables simulation of long-duration processes previously intractable with full CFD–DEM, including particle mixing and segregation, population balance modeling of granulation and agglomeration, and thermal processing with species transport. For these applications, pseudo-steady flow statistics recur over time scales far longer than individual bubble passage events, making rCFD ideally suited for industrial process simulation.

The computational efficiency of the rCFD time extrapolation method represents a transformative advancement for fluidized bed simulations, as illustrated in Fig. 13. Traditional CFD–DEM simulations required 16,200 s (4.5 h) of wall-clock time to simulate just 1 s of physical process time, whereas the rCFD approach achieved equivalent predictions in only 4 s through time extrapolation, a remarkable speed-up factor of 4050×.

This dramatic reduction in computational cost fundamentally changes the scope of feasible simulation studies: parametric investigations requiring dozens of cases, long-term steady-state analyses spanning multiple seconds, and real-time process monitoring applications that were previously intractable with CFD–DEM become readily accessible with rCFD. For instance, simulating 10 s of fluidized bed

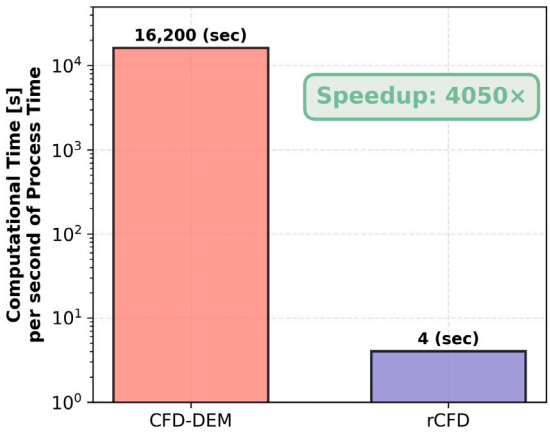

Fig. 13. Computational cost for rCFD and CFD–DEM simulations.

operation to establish steady-state bubble dynamics would require approximately 45 h using conventional CFD–DEM, but can be completed in under one minute with rCFD.

The computational speed-up enables a new paradigm of rapid digital twin development for fluidized bed systems, facilitating iterative design optimization and uncertainty quantification studies that leverage hundreds or thousands of simulation evaluations.

5. Conclusion

This study validated CFD–DEM simulations against non-invasive MRI measurements of gas–solid fluidized bed dynamics and demonstrated the viability of recurrence-based CFD (rCFD) for computationally efficient time extrapolation. Three key contributions emerge from this work:

Comprehensive drag model validation against full-field MRI data identified the Koch & Hill correlation as the most consistent performer across multiple metrics. While all four tested drag models (Koch & Hill, Di Felice, Gidaspow, Beetstra) predicted mean bed heights within experimental uncertainty (±1 cm), the Koch & Hill model demonstrated better agreement with temporal expansion dynamics, bubble size distributions throughout the bed height, bubble velocity statistics, and radial particle distribution patterns compared to the other models evaluated. All models systematically underpredicted small bubbles (diameter <7.5 mm) near the distributor, indicating that uniform velocity inlet boundary conditions do not adequately represent the flow field downstream of porous distributor plates. Investigation of void-fraction-corrected inlet conditions (*consistentSuperficialVelocityInlet*) produced minimal improvement, suggesting that resolved distributor-region modeling or empirically calibrated inlet conditions merit future investigation.

MRI measurements provided internal flow validation data that complemented CFD–DEM predictions, enabling quantitative comparison of bubble formation, growth, coalescence patterns, and particle segregation without flow disturbance. The vertical MRI system at TUHH captured flow fields at 4 mm by 8 mm spatial and 20 ms temporal resolution across the full 96 mm diameter bed. However, MRI data requires substantial post-processing including signal thresholding, artifact removal, and binary image conversion, each introducing potential systematic errors. The threshold selection procedure employed in this work used multi-criteria optimization with bootstrap uncertainty quantification to minimize these effects, but absolute validation remains challenging. Additionally, MRI measurements commenced several minutes after fluidization startup to ensure steady-state conditions, precluding direct time-synchronized comparison with CFD–DEM or rCFD predictions. Despite these limitations, the statistical agreement between MRI and simulation data across bed expansion dynamics, bubble statistics, and radial distributions provides confidence in the validated modeling approach.

Transport-based rCFD achieved a 4050× computational speed-up while preserving statistical flow features observed in both CFD–DEM simulations and MRI measurements. Time extrapolation from 5 s of CFD–DEM input to 10 s of predicted behavior maintained bed expansion dynamics, bubble size distributions, velocity statistics, and radial profiles without drift or spurious behavior. FFT analysis identified a characteristic recurrence period (τ_{p-p}) of 0.27 s at 1.5 U_{mf}, enabling reconstruction with 0.01 s recurrence time steps (τ_{crit}) from Eq. (13). This computational efficiency transforms the scope of feasible simulation studies: parametric investigations requiring dozens of operating conditions, long-term steady-state analyses, and uncertainty quantification studies involving hundreds of evaluations become tractable. However, rCFD fundamentally relies on pseudo-repetitive flow behavior; systems exhibiting pronounced transient dynamics, such as startup, shutdown, or load changes cannot be extrapolated from a single steady-state database. Simulation of such transient regimes requires multiple CFD–DEM databases spanning the relevant operating conditions, together with appropriate interpolation strategies to transition between flow states. Development of robust database interpolation approaches represents an important direction for extending rCFD applicability to dynamic industrial processes.

The approach demonstrated here is generalizable to other multiphase systems exhibiting pseudo-periodic behavior, including bubble columns, spouted beds, and circulating fluidized beds. However, several limitations warrant acknowledgment. The current study focused on spherical particles (poppy seeds) with a narrow size distribution at moderate Reynolds numbers. Extension to polydisperse systems with size-dependent segregation, non-spherical particles with orientation-dependent drag, and high-velocity transport regimes requires additional validation. Integration of rCFD with population balance models for coupled flow-particle property evolution represents a promising direction for predicting product quality in industrial granulation and coating applications, though such coupling remains to be demonstrated.

Nomenclature

Greek symbols

α	Phase void fraction, –
β	Drag force coefficient, kg/(m^3 s)
γ	Field quantity (gas void fraction), –
μ	Dynamic viscosity, Pa s
μ_H	Mean bed expansion height, m
ν	Kinematic viscosity, m^2/s
ρ	Density, kg/m^3
σ_H	Standard deviation of bed height, m
τ_{rec}	Characteristic recurrence period, s
τ	Net torque, N m
ζ	Di Felice drag model parameter, –
ω	Angular velocity, rad/s

Latin symbols

A	Bubble area, mm^2
A'	Projected area of particles, m^2
C_D	Drag coefficient, –
c_n, c_t	Normal and tangential damping coefficients, –
CV	Coefficient of variation, %
D	Bed diameter, m
d_p	Particle diameter, m
d_{32}	Sauter mean diameter of particles, m
e	Coefficient of restitution, –
$\mathbf{F}$	Force, N

h	Bubble height, mm
$H_{\text{expansion}}$	Bed expansion height, cm
I	Moment of inertia, kg m^2
k_n, k_t	Normal and tangential spring stiffnesses, N/m
k_{fr}	Coefficient of friction, –
L_h	Hydrodynamic entrance length, m
m	Mass, kg
N_{α_g}	Normalization factor for recurrence plot, –
p	Pressure, Pa
Q	Volumetric flow rate, m^3/s
R	Pipe radius, m
Re	Reynolds number –
s	Poisson's ratio, –
t	Time, s
$\mathbf{u}_g$	Gas velocity vector in a computational cell, m/s
u_{in}	Superficial inlet velocity, m/s
u_{mf}	Minimum fluidization velocity, m/s
V	Volume, flow domain, m^3
$\mathbf{v}_i$	Velocity of particle i, m/s
w	Bubble width, mm
x, y, z	Spatial coordinates, m
Y	Young's modulus, Pa

Dimensionless numbers

Co	Courant number, –
Re	Reynolds number, –

Subscripts and superscripts

g	Gas phase
i,j	Particle index
p,P	Particle
rec	Recurrence
s	Solid phase
$static$	Static bed
t	Turbulent
$threshold$	Threshold value
W	Wall
$P-P$	Particle–particle
$P-W$	Particle–wall

Abbreviations

CFD	Computational fluid dynamics
CFD–DEM	Computational fluid dynamics–discrete element method
CT	Computed tomography
CV	Coefficient of variation
DEM	Discrete element method
ECT	Electrical capacitance tomography
EPSD	Elastic–plastic spring-dashpot
FFT	Fast Fourier transform
HPC	High performance cluster
KS	Kolmogorov–Smirnov
MRI	Magnetic resonance imaging
NRMSE	Normalized root mean square error
piDMD	Physics-informed dynamic mode decomposition
PIV	Particle image velocimetry
POD	Proper orthogonal decomposition
RANS	Reynolds-averaged Navier–Stokes
rCFD	Recurrence-based computational fluid dynamics

CRediT authorship contribution statement

Asif Shaik: Writing – original draft, Visualization, Validation, Software, Methodology, Investigation, Formal analysis, Data curation, Conceptualization. **Swantje Pietsch-Braune:** Writing – review & editing, Supervision, Project administration, Methodology, Investigation, Conceptualization. **Stefan Pirker:** Writing – review & editing, Software, Methodology, Conceptualization. **Melis Özdemir:** Writing – original draft, Methodology, Investigation. **Muhammad Adrian:** Methodology. **Alexander Penn:** Writing – review & editing, Validation, Methodology. **Stefan Heinrich:** Writing – review & editing, Supervision, Resources, Methodology, Investigation, Conceptualization.

Declaration of Generative AI and AI-assisted technologies in the writing process

During the preparation of this work, the authors used Claude (Anthropic) and ChatGPT (OpenAI) to improve the clarity, grammar, and structure of the manuscript text. Specifically, AI tools were employed for: (1) language editing and grammar correction, (2) restructuring sentences and paragraphs for improved readability, (3) ensuring consistency in technical terminology and notation, and (4) formatting LaTeX code. All scientific content, methodology, results interpretation, and conclusions were developed independently by the authors. AI tools were not used for data analysis, figure generation, experimental design, or scientific decision-making. After using these tools, the authors reviewed and edited the content as needed and take full responsibility for the content of the published article.

Funding

This project is funded by the Deutsche Forschungsgemeinschaft (DFG, German Research Foundation) – CRC 1615 – 503850735. Moreover, the authors gratefully acknowledge partial funding of this project by Deutsche Forschungsgemeinschaft (DFG, German Research Council) under project number 471615686.

Declaration of competing interest

The authors declare that they have no known competing financial interests or personal relationships that could have appeared to influence the work reported in this paper.

The author is an Editorial Board Member/Editor-in-Chief/Associate Editor/Guest Editor for this journal and was not involved in the editorial review or the decision to publish this article.

Acknowledgment

The authors thank Nick Hildebrandt (researcher from the Institute of Solids Process Engineering and Particle Technology, Hamburg University of Technology) for providing the poppy seed material properties used in CFD–DEM simulations.

Data availability

The data that support the findings of this study, including CFD–DEM simulation results, MRI experimental measurements, and post-processing scripts, will be openly available in TORE (TUHH Open Research Repository) at https://hdl.handle.net/11420/57789 upon publication.

The persistent identifier (DOI) is https://doi.org/10.15480/882.15949.

References

Agrawal, V., Shinde, Y., Shah, M.T., Utikar, R.P., Pareek, V.K., Joshi, J.B., 2018. Effect of drag models on CFD–DEM predictions of bubbling fluidized beds with Geldart D particles. Adv. Powder Technol. 29 (11), 2658–2669.

Akhtar, I., Nayfeh, A.H., Ribbens, C.J., 2009. On the stability and extension of reduced-order Galerkin models in incompressible flows: a numerical study of vortex shedding. Theor. Comput. Fluid Dyn. 23, 213–237.

Atxutegi, A., Kieckhefen, P., Pietsch, S., Aguado, R., Olazar, M., Heinrich, S., 2021. Unresolved CFD-DEM simulation of spherical and ellipsoidal particles in conical and prismatic spouted beds. Powder Technol. 389, 493–506.

Azmir, J., Hou, Q., Yu, A., 2020. CFD-DEM study of the effects of food grain properties on drying and shrinkage in a fluidised bed. Powder Technol. 360, 33–42.

Baddoo, P.J., Herrmann, B., McKeon, B.J., Nathan Kutz, J., Brunton, S.L., 2023. Physics-informed dynamic mode decomposition. Proc. R. Soc. A 479 (2271), 20220576.

Beetstra, R., van der Hoef, M.A., Kuipers, J., 2007. Drag force of intermediate Reynolds number flow past mono-and bidisperse arrays of spheres. AIChE J. 53 (2), 489–501.

Cai, Q., Lee, B., Ong, S., Hu, J., 2020. Fluidized-bed fenton technologies for recalcitrant industrial wastewater treatment-Recent advances, challenges and perspective. Water Res. 190, 116692. http://dx.doi.org/10.1016/j.watres.2020.116692.

Che, H., Al-Shemmeri, M., Fryer, P.J., Lopez-Quiroga, E., Wheldon, T.K., Windows-Yule, K., 2023. PEPT validated CFD-DEM model of aspherical particle motion in a spouted bed. Chem. Eng. J. 453, 139689.

Chew, J., LaMarche, W., Cocco, R., 2022. 100 years of scaling up fluidized bed and circulating fluidized bed reactors. Powder Technol. http://dx.doi.org/10.1016/j.powtec.2022.117813.

Clarke, D.A., Hogendoorn, W., Penn, A., Serial, M.R., 2025. Magnetic resonance imaging in granular flows: An overview of recent advances. Particuology 101, 18–32.

Cundall, P.A., Strack, O.D., 1979. A discrete numerical model for granular assemblies. Geotechnique 29 (1), 47–65.

da Silva, C.A.M., Butzge, J.J., Nitz, M., Taranto, O.P., 2014. Monitoring and control of coating and granulation processes in fluidized beds–A review. Adv. Powder Technol. 25 (1), 195–210.

Dabbagh, F., Pirker, S., Schneiderbauer, S., 2020. On the fast modeling of species transport in fluidized beds using recurrence computational fluid dynamics. AIChE J. 66 (5), e16931.

Darweesh, A.H., Weis, M.M., 2024. The impact of particle size in fluidized bed on heat transfer behavior: A review. Adv. Mech. Mater. Eng. http://dx.doi.org/10.7862/rm.2024.4.

De Munck, M., Peters, E., Kuipers, J., 2023. CFD-DEM fluidized bed drying study using a coarse-graining technique. Ind. Eng. Chem. Res. 62 (48), 20911–20920.

Deen, N., Annaland, M.V.S., Van der Hoef, M.A., Kuipers, J., 2007. Review of discrete particle modeling of fluidized beds. Chem. Eng. Sci. 62 (1–2), 28–44.

Department of Particulate Flow Modelling, Johannes Kepler University, 2024. CFDEM®coupling: An academic adaptation. Linz, Austria, https://github.com/ParticulateFlow/CFDEMcoupling-PFM.

Di Felice, R., 1994. The voidage function for fluid-particle interaction systems. Int. J. Multiph. Flow 20 (1), 153–159.

Eckmann, J.-P., Kamphorst, S.O., Ruelle, D., et al., 1995. Recurrence plots of dynamical systems. World Sci. Ser. Nonlinear Sci. Ser. A 16, 441–446.

Gidaspow, D., 1994. Multiphase Flow and Fluidization: Continuum and Kinetic Theory Descriptions. Academic Press.

Golshan, S., Sotudeh-Gharebagh, R., Zarghami, R., Mostoufi, N., Blais, B., Kuipers, J., 2020. Review and implementation of CFD-DEM applied to chemical process systems. Chem. Eng. Sci. 221, 115646.

Grohn, P., Lawall, M., Oesau, T., Heinrich, S., Antonyuk, S., 2020. CFD-DEM simulation of a coating process in a fluidized bed rotor granulator. Processes 8 (9), 1090.

Guío-Pérez, D.C., Bonmann, M., Bryllert, T., Seemann, M., Stake, J., Johnsson, F., Pallarès, D., 2023. Radar-based measurements of the solids flow in a circulating fluidized bed. Fuel http://dx.doi.org/10.1016/j.fuel.2023.128232.

Guo, X., Liu, G., Zhao, J., Wang, R., He, Y., 2021. Investigation of gas-solid flows in a spout fluidized bed on drag and solid stress: Cfd-dem, tfm, and experimental validation. J. Chem. Eng. Res. Updates 8, 1–23.

Han, C., Fu, X., Guo, X., Lu, W., Zhang, S., Wang, H., Yang, Y., 2024. Computational fluid dynamics–discrete element method numerical investigation of binary particle mixing in gas–solid fluidized bed with different drag models. Water 16 (22), 3210.

Heinrich, S., Peglow, M., Ihlow, M., Henneberg, M., Mörl, L., 2002a. Analysis of the start-up process in continuous fluidized bed spray granulation by population balance modelling. Chem. Eng. Sci. 57 (20), 4369–4390.

Heinrich, S., Peglow, M., Ihlow, M., Mörl, L., 2003. Particle population modeling in fluidized bed-spray granulation—analysis of the steady state and unsteady behavior. Powder Technol. 130 (1–3), 154–161.

Heinrich, S., Peglow, M., Mörl, L., 2002b. Unsteady and steady-state particle size distributions in batch and continuous fluidized bed granulation systems. Chem. Eng. J. 86 (1–2), 223–231.

Hill, R.J., Koch, D.L., Ladd, A.J., 2001. Moderate-Reynolds-number flows in ordered and random arrays of spheres. J. Fluid Mech. 448, 243–278.

Jiang, S., Wu, K., Francia, V., Ouyang, Y., Coppens, M.-O., 2024. Machine learning assisted experimental characterization of bubble dynamics in gas–solid fluidized beds. Ind. Eng. Chem. Res. 63 (19), 8819–8832.

Jourdan, N., Neveux, T., Potier, O., Kanniche, M., Wicks, J., Nopens, I., Rehman, U., Le Moullec, Y., 2019. Compartmental Modelling in chemical engineering: A critical review. Chem. Eng. Sci. 210, 115196.

Jung, S.K., Shin, S., Myong, R.S., Cho, T.H., 2011. An efficient CFD-based method for aircraft icing simulation using a reduced order model. J. Mech. Sci. Technol. 25, 703–711.

Kanholy, S.K., Battaglia, F., 2012. Eulerian-Eulerian modeling of multiple jet interactions for different distributor plates. In: Fluids Engineering Division Summer Meeting. Vol. 44755, American Society of Mechanical Engineers, pp. 645–652.

Kieckhefen, P., Lichtenegger, T., Pietsch, S., Pirker, S., Heinrich, S., 2019. Simulation of spray coating in a spouted bed using recurrence CFD. Particuology 42, 92–103.

Kieckhefen, P., Pietsch, S., Dosta, M., Heinrich, S., 2020. Possibilities and limits of computational fluid dynamics–discrete element method simulations in process engineering: A review of recent advancements and future trends. Annu. Rev. Chem. Biomol. Eng. 11 (1), 397–422.

Kieckhefen, P., Pietsch-Braune, S., Heinrich, S., 2022. Product-property guided scale-up of a fluidized bed spray granulation process using the CFD-DEM method. Processes 10 (7), 1291.

Kloss, C., Goniva, C., Hager, A., Amberger, S., Pirker, S., 2012. Models, algorithms and validation for opensource DEM and CFD–DEM. Prog. Comput. Fluid Dyn. an Int. J. 12 (2–3), 140–152.

Ku, X., Li, T., Løvås, T., 2015. CFD–DEM simulation of biomass gasification with steam in a fluidized bed reactor. Chem. Eng. Sci. 122, 270–283.

Lan, B., Zhao, P., Xu, J., Zhao, B., Zhai, M., Wang, J., 2022. CFD-DEM-IBM simulation of particle drying processes in gas-fluidized beds. Chem. Eng. Sci. 255, 117653.

Launder, B.E., Spalding, D.B., 1983. The numerical computation of turbulent flows. In: Numerical Prediction of Flow, Heat Transfer, Turbulence and Combustion. Elsevier, pp. 96–116.

Lei, H., Zhu, L.-T., Luo, Z.-H., 2023. CFD-DEM study of reactive gas-solid flows with cohesive particles in a high temperature polymerization fluidized bed. Chem. Eng. Sci. 268, 118437.

Li, X., Wang, S., Kong, D., Luo, K., Fan, J., 2024. Data-driven reduced-order model for bubbling fluidized beds. Ind. Eng. Chem. Res. 63 (3), 1634–1648.

Lichtenegger, T., Kieckhefen, P., Heinrich, S., Pirker, S., 2019. Dynamics and long-time behavior of gas–solid flows on recurrent-transient backgrounds. Chem. Eng. J. 364, 562–577.

Lichtenegger, T., Peters, E., Kuipers, J., Pirker, S., 2017. A recurrence CFD study of heat transfer in a fluidized bed. Chem. Eng. Sci. 172, 310–322.

Lichtenegger, T., Pirker, S., 2016. Recurrence CFD–a novel approach to simulate multiphase flows with strongly separated time scales. Chem. Eng. Sci. 153, 394–410.

Liu, M., Zhang, Y., Bi, H., Grace, J.R., Zhu, Y., 2010. Non-intrusive determination of bubble size in a gas–solid fluidized bed: An evaluation. Chem. Eng. Sci. 65 (11), 3485–3493.

Lucia, D.J., Beran, P.S., Silva, W.A., 2004. Reduced-order modeling: new approaches for computational physics. Prog. Aerosp. Sci. 40 (1–2), 51–117.

Lumetzberger, H., Pirker, S., Lichtenegger, T., 2025. Propagator-moments approximation for recurrence CFD: Application to species transport in turbulent flows. Chem. Eng. Sci. 311, 121624.

Marchelli, F., Hou, Q., Bosio, B., Arato, E., Yu, A., 2020. Comparison of different drag models in CFD-DEM simulations of spouted beds. Powder Technol. 360, 1253–1270.

Munck, M.D., Peters, E., Kuipers, J., 2023. Fluidized bed gas-solid heat transfer using a CFD-DEM coarse-graining technique. Chem. Eng. Sci. http://dx.doi.org/10.1016/j.ces.2023.119048.

Okhovat-Alavian, S., Behin, J., Mostoufi, N., 2020. Investigating bubble dynamics in a semi-cylindrical gas-solid fluidized bed. Powder Technol. 370, 129–136.

Pant, P., Doshi, R., Bahl, P., Barati Farimani, A., 2021. Deep learning for reduced order modelling and efficient temporal evolution of fluid simulations. Phys. Fluids 33 (10).

Penn, A., Tsuji, T., Brunner, D.O., Boyce, C.M., Pruessmann, K.P., Müller, C.R., 2017. Real-time probing of granular dynamics with magnetic resonance. Sci. Adv. 3 (9), e1701879.

Pigford, R.L., 1968. Fluidized particles. By J. F. DAVIDSON and D. HARRISON. Cambridge University Press, 1963. 155 pp. 35s. J. Fluid Mech. 33 (3), 623–624.

Pirker, S., Atzori, M., Heinrich, S., Lichtenegger, T., 2025. Particle size segregation in bi and penta-disperse gas–solid fluidized beds: CFD-DEM and recurrence CFD simulations. Chem. Eng. Sci. 309, 121469.

Pirker, S., Lichtenegger, T., 2018. Efficient time-extrapolation of single-and multiphase simulations by transport based recurrence CFD (rCFD). Chem. Eng. Sci. 188, 65–83.

Raveh, D.E., 2001. Reduced-order models for nonlinear unsteady aerodynamics. AIAA J. 39 (8), 1417–1429.

Sasic, S., Johnsson, F., Leckner, B., 2006. Inlet boundary conditions for the simulation of fluid dynamics in gas–solid fluidized beds. Chem. Eng. Sci. 61, 5183–5195.

Sen, M., Barrasso, D., Singh, R., Ramachandran, R., 2014. A multi-scale hybrid CFD-DEM-PBM description of a fluid-bed granulation process. Processes 2 (1), 89–111.

Sutkar, V.S., Deen, N.G., Patil, A.V., Salikov, V., Antonyuk, S., Heinrich, S., Kuipers, J., 2016. CFD–DEM model for coupled heat and mass transfer in a spout fluidized bed with liquid injection. Chem. Eng. J. 288, 185–197.

Tu, Q., Luo, Z., Wang, H., 2021. MP-PIC simulation of the gas-solid full-loop flow characteristics in a dual fluidized bed and validation with experimental data. Chem. Eng. J. 421, 129835. http://dx.doi.org/10.1016/J.CEJ.2021.129835.

Wang, S., Luo, K., Hu, C., Lin, J., Fan, J., 2019. CFD-DEM simulation of heat transfer in fluidized beds: Model verification, validation, and application. Chem. Eng. Sci. 197, 280–295.

Wang, J., Shao, Y., Yan, X., Zhu, J., 2020. Review of (gas)-liquid-solid circulating fluidized beds as biochemical and environmental reactors. Chem. Eng. J. 386, 121951. http://dx.doi.org/10.1016/J.CEJ.2019.121951.

Wang, S., Shen, Y., 2022. Coarse-grained CFD-DEM modelling of dense gas-solid reacting flow. Int. J. Heat Mass Transfer http://dx.doi.org/10.1016/j.ijheatmasstransfer.2021.122302.

Wang, T., Wang, S., Shen, Y., 2021. Particle-scale study of gas-solid flows in a bubbling fluidised bed: Effect of drag force and collision models. Powder Technol. 384, 353–367.

Watson, B., Lindmüller, L., Heinrich, S., Theuerkauf, J., Yao, Y., Fan, Y., 2024. Dynamic bubble tracking in fluidized beds via electrical capacitance volume tomography. Chem. Eng. J. 487, 150461.

Weber, B., von Campenhausen, M., Maßmann, T., Bednarz, A., Jupke, A., 2019. CFD based compartment-model for a multiphase loop-reactor. Chem. Eng. Sci.: X 2, 100010.

Wu, C., Yang, H., He, X., Hu, C., Yang, L., Li, H., 2022. Principle, development, application design and prospect of fluidized bed heat exchange technology: Comprehensive review. Renew. Sustain. Energy Rev. http://dx.doi.org/10.1016/j.rser.2021.112023.

Yan, Y., 2016. Non-intrusive measurement and hydrodynamics characterization of gas2013solid fluidized beds: a review. Meas. Sci. Technol. 27, http://dx.doi.org/10.1088/0957-0233/27/11/112001.

Zapater, D., Kulkarni, S., Wéry, F., Cui, M., Herguido, J., Menendez, M., Heynderickx, G.J., Geem, K.V., Gascon, J., Castaño, P., 2024. Multifunctional fluidized bed reactors for process intensification. Prog. Energy Combust. Sci. http://dx.doi.org/10.1016/j.pecs.2024.101176.

Zhang, K., Wang, S., Li, B., He, Y., Zhao, Y., 2020. Heat transfer in a pulsed fluidized bed by using coupled CFD-DEM method. Powder Technol. 367, 497–505.

Zhao, Z., Zhou, L., Bai, L., Wang, B., Agarwal, R.K., 2023. Recent advances and perspectives of CFD2013DEM simulation in fluidized bed. Arch. Comput. Methods Eng. http://dx.doi.org/10.1007/s11831-023-10001-6.

Zhao, Z., Zhou, L., Bai, L., Wang, B., Agarwal, R., 2024. Recent advances and perspectives of CFD–DEM simulation in fluidized bed. Arch. Comput. Methods Eng. 31 (2), 871–918.

Zhong, H., Xiong, Q., Yin, L., Zhang, J., Zhu, Y., Liang, S., Niu, B., Zhang, X., 2020. CFD-based reduced-order modeling of fluidized-bed biomass fast pyrolysis using artificial neural network. Renew. Energy 152, 613–626.

Zhou, Z., Kuang, S., Chu, K., Yu, A., 2010. Discrete particle simulation of particle–fluid flow: model formulations and their applicability. J. Fluid Mech. 661, 482–510.

Zhou, L., Lv, W., Bai, L., Han, Y., Wang, J., Shi, W., Huang, G., 2022. CFD2013DEM study of gas2013solid flow characteristics in a fluidized bed with different diameter of coarse particles. Energy Rep. http://dx.doi.org/10.1016/j.egyr.2022.01.174.

Zhou, L., Zhang, L., Bai, L., Shi, W., Li, W., Wang, C., Agarwal, R., 2017. Experimental study and transient CFD/DEM simulation in a fluidized bed based on different drag models. RSC Adv. 7 (21), 12764–12774.